Remote Sensing of Environment 143 (2014) 192–203

Contents lists available at ScienceDirect

Remote Sensing of Environment

journal homepage: www.elsevier.com/locate/rse

Monitoring snow cover using Chinese meteorological satellite data over China

Juntao Yang [a], Lingmei Jiang [a,*], Jiancheng Shi [b], Shengli Wu [c], Ruijing Sun [c], Hu Yang [d]

[a] State Key Laboratory of Remote Sensing Science, Research Center for Remote Sensing and GIS, and School of Geography, Beijing Normal University, Beijing 100875, China
[b] State Key Laboratory of Remote Sensing Science, Institute of Remote Sensing and Digital Earth, Chinese Academy of Sciences, Beijing 100101, China
[c] National Satellite Meteorological Center, Beijing 100081, China
[d] Earth Science System Interdisciplinary Center, University of Maryland, College Park, MD 20742, USA

ARTICLE INFO

Article history:
Received 31 May 2013
Received in revised form 26 December 2013
Accepted 27 December 2013
Available online 29 January 2014

Keywords:
FY-2D/E VISSR
FY-3B MWRI
Snow cover
Geostationary satellite
China

ABSTRACT

Snow cover plays an important role in hydrological processes and global climate change research. Geostationary satellites with high temporal resolution provide multiple observations in one day, which highlights their potential for monitoring real-time snow-cover information. In this paper, data from the Chinese meteorological satellites Fengyun-2D (FY-2D), Fengyun-2E (FY-2E) and Fengyun-3B (FY-3B) was used for snow-cover mapping over China. A new method of detecting snow-cover information is proposed, that combines the Visible and Infrared Spin Scan-Radiometer (VISSR) on board the geostationary satellites FY-2D and FY-2E and the Microwave Radiation Imager (MWRI) on board the polar orbiting satellite FY-3B. The snow cover estimated from Fengyun satellites was compared by the Moderate Resolution Imaging Spectroradiometer (MODIS) snow-cover products (MOD10A1 and MYD10A1), and Interactive Multisensor Snow and Ice Mapping System (IMS) snow-cover products. The Fengyun satellite snow-cover images and IMS snow-cover products were validated with meteorological station observations for the 2010–2011 and 2011–2012 winter seasons. The influence of elevation and land-cover types on the accuracy of snow retrievals was also analyzed. The results showed that the combined use of FY-2D and FY-2E VISSR data reduced cloud obscuration by 30.47% compared to the MODIS products. The validation demonstrated that the accuracy of the final multi-sensor snow-cover images was 91.28%, which is similar to that for IMS snow-cover products. This work indicates that combined data from geostationary satellites and passive microwave remote sensing monitored snow cover over China to a high level of accuracy.

1. Introduction

Seasonal snow cover plays an important role in hydrological processes, surface radiation and climates. Snow-cover mapping has been utilized in operational snowmelt, runoff forecasting, data assimilation and the calibration or validation of various hydrological models (Gao, Xie, Lu, Yao, & Liang, 2010). In situ observations are the traditional source of information on the snow cover. However, it does not fully satisfy the needs of the modeling community (Romanov & Tarpley, 2007). With a growing number of satellite platforms, satellite remote sensing technology has been used to monitor snow cover at both regional and global scales. It has become possible to monitor snow cover in near real time.

Both optical and passive microwave imagery can be used to extract snow cover information. The Advanced Very High Resolution Radiometer (AVHRR) on board the National Oceanic and Atmospheric Administration (NOAA) polar orbiter, the Moderate Resolution Imaging Spectroradiometer (MODIS) on board the Terra and Aqua satellites, the Special Sensor Microwave Imager (SSM/I) on board the Defense Meteorological Satellite Platform (DMSP), and Landsat Thematic Mapper (TM) have been widely used to monitor snow cover (Allen, Durkee, & Wash, 1990; Dozier & Painter, 2004; Grody & Basist, 1996; Hall, Riggs, Salomonson, DiGirolamo, & Bayr, 2002). Monitoring snow cover using optical imagery with high spatial resolution is seriously hampered by cloud cover because of the similar spectral reflectance of snow and some types of clouds (Liang et al., 2008; Wang, Xie, & Liang, 2008). MODIS snow-cover products composed over eight days may be used to reduce cloud obscuration. However, timely snow-cover mapping is required to identify disaster regions and in hydrological applications. Therefore, various approaches have been proposed to reduce cloud obscuration by altering the cloud mask, separating cloud-masked pixels, and applying spatial–temporal or multi-sensor combinations (Gao et al., 2010; Hall, Riggs, Foster, & Kumar, 2010; Parajka & Blöschl, 2008). Passive microwave remote sensing presents the advantages of penetrating cloud cover and obtaining more snow-cover information. However, the coarse spatial resolution of passive microwave data is still its main limitation. In addition, current passive microwave snow algorithms cannot detect wet and shallow snow. The wet snow cover and

* Corresponding author at: State Key Laboratory of Remote Sensing Science, Research Center for Remote Sensing and GIS, and School of Geography, Beijing Normal University, Beijing 100875, China.
E-mail address: jiang@bnu.edu.cn (L. Jiang).

0034-4257/$ – see front matter © 2014 Elsevier Inc. All rights reserved.
http://dx.doi.org/10.1016/j.rse.2013.12.022

serious cloud obscuration in southern China has indicated the limitation of using optical or passive microwave remote sensing data separately.

Because there are only one–two observations per day of polar-orbiting satellites, substantial cloud obscuration is the main limitation of daily optical snow cover products. In daily snow-cover mapping, the most effective method of reducing cloud obscuration is to increase the number of observations within a day. Geostationary satellites provide frequent observations, which allow for monitoring an entire hemisphere at temporal resolution in close to real time (Wildt, Seiz, & Gruen, 2007). Current operational geostationary satellites include Geostationary Operational Environmental Satellites (GOES), Meteosat Second Generation (MSG), Multi-functional Transport Satellite-2 (MTSAT-2) and Fengyun-2 (FY-2). GOES data for snow-cover mapping was used by Romanov, Gutman, and Csiszar (2000, 2003), who made a daily composite image and obtained daily snow-cover images. For MSG, Wildt et al. (2007) used temporal differences between images to produce daily snow-cover maps. Siljamo and Hyvärinen (2011) developed a new snow algorithm for MSG, based on scatterplots and classification rules. Oyoshi, Takeuchi, and Yasuoka (2007) used MTSAT data for snow-cover mapping and found that the maps were consistent with those from AVHRR and MODIS. FY-2C satellite data was used by Li, Yan, and Liu (2007) to derive snow-cover information using different threshold criteria. Currently, most methods for snow-cover detection based on geostationary satellite data utilize spectral-based threshold algorithms. Cloud obscuration can be reduced by utilizing multi-temporal geostationary satellite data. Currently, daily snow-cover monitoring techniques that use either optical sensors on polar orbiting satellites or passive microwave sensors cannot provide accurate daily snow-cover images with low cloud obscuration. Therefore, the combined use of optical sensors on board geostationary satellites and passive microwave sensors will provide more surface information without cloud obscuration.

In daily snow-cover mapping, the most effective method of reducing cloud obscuration is to increase the number of observations within a day (e.g., see Wang et al., 2008). In addition, multi-sensor technology can also be used to obtain more accurate information on snow cover. This paper describes a snow-cover mapping algorithm that uses data from two geostationary satellites (FY-2D, FY-2E) combined with passive microwave data derived from polar-orbiting meteorological satellite FY-3B. Despite the different observation times and locations for FY-2D and FY-2E, the data from both satellites was utilized to monitor snow cover with less cloud obscuration during in the period of one day, with the observation frequency reduced to half an hour.

In Section 2, the Fengyun satellite data, ground observations and other snow-cover products are compared. Section 3 presents the methodology, including data pre-processing, development of a snow-cover algorithm, and techniques for reducing cloud obscuration. Section 4 details the comparison and validation of FY-2D/E, MODIS and IMS snow-cover products, and the conclusion appears in the final section.

2. Data

2.1. In situ measurements

The China Meteorological Administration (CMA) provides daily meteorological observations for the whole of China, including snow depth, and minimum, maximum and mean air temperatures, along with other information. In this study, a total of 699 meteorological stations over China were used in the validation. Snow depth observations were also used in the development of a snow-cover algorithm. Global 30 Arc-Second Elevation (GTOPO30) is a global digital elevation model (DEM). The spatial resolution of GTOPO30 is approximately 1 km (USGS, 1996). Fig. 1 is a map showing the locations of the meteorological stations, and the DEM derived from GTOPO30 is overlaid on the map.

2.2. Satellite data

The FY-2 series are first-generation Chinese geostationary meteorological satellites. Currently, the FY-2D and FY-2E satellites are operational, and FY-2F is on standby. FY-2D was launched at central

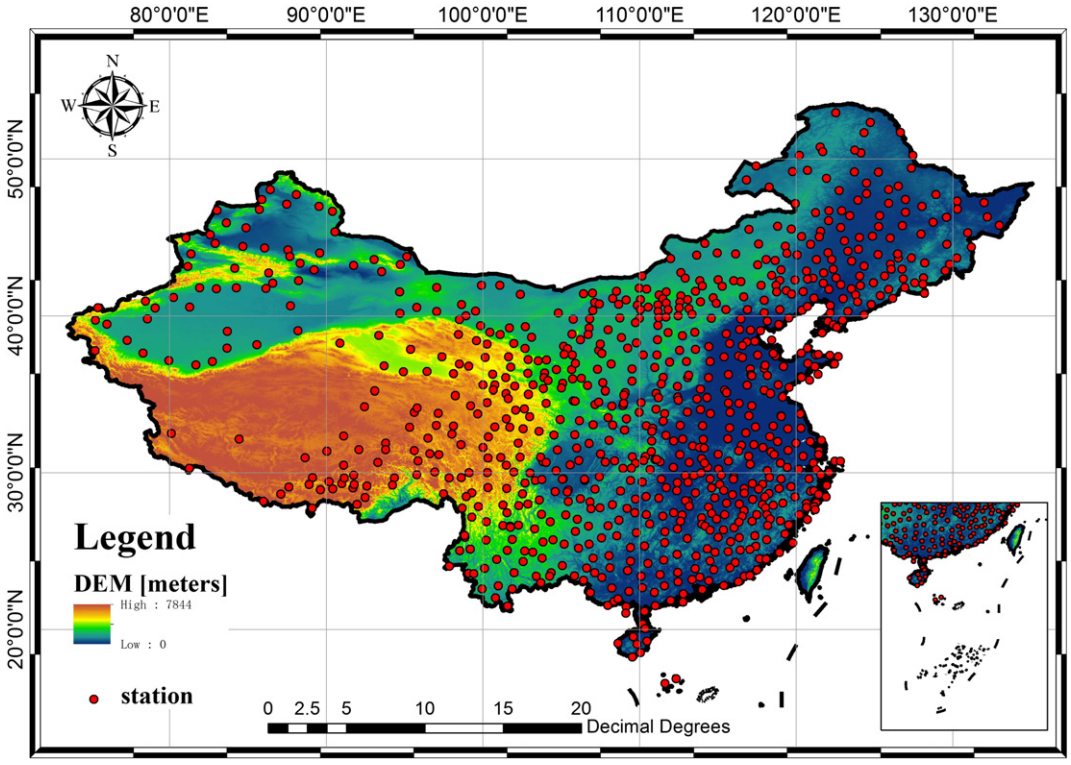

Fig. 1. Meteorological stations and DEM of China.

longitude 86.5° E on December 8, 2006, and FY-2E at central longitude 104.5° E was launched on June 15, 2008. The Visible and Infrared Spin-Scan Radiometers (VISSR) on board FY-2D and FY-2E are five-band sensors, comprising one visible band and four infrared bands. The temporal resolution of VISSR is 1 h in normal operational mode and half an hour in special operational mode, which is required for instance in the flood season. The imaging time difference of these two satellites is half an hour. Table 1 lists detailed information about VISSR. The characteristics of VISSR are similar to those on board the GOES and MTSAT-2 satellites, except for a coarser (6-bit) radiometric resolution in the visible band.

FY-3B was launched on November 5, 2010. It is an afternoon polar orbiting satellite which crosses the equator at the ascending node at 13:30 local time. The Microwave Radiation Imager (MWRI) on board FY-3B is a passive microwave imager that scans the earth with a conical at viewing angle of 53° and has a swath width of 1400 km. It is a total-power passive radiometer which measures the radiation at the five frequencies 10.65, 18.7, 23.8, 36.5 and 89.0 GHz with dual polarization (Yang, Lv, Xu, He, & Wu, 2011). Because the data from FY-2D, FY-2E VISSR and FY-3B MWRI may be simultaneously obtained from CMA, they were all used for snow-cover mapping in this study. Because FY-2D and FY-2E provide multiple observations in one day, potentially they can obtain more surface information with less cloud obscuration; FY-3B MWRI data was also used for snow-cover mapping in cloud-obscured conditions.

2.3. Snow-cover products used for comparisons

In this study, MODIS daily snow-cover products were used for comparison with FY-2D/E images. MODIS Terra/Aqua Snow Cover Daily L3 Global 500 m SIN GRID V005 (MOD10A1, MYD10A1) products (Hall & Riggs, 2007) and the Interactive Multisensor Snow and Ice Mapping System (IMS) snow-cover products were used for comparison. IMS is a satellite image analysis and processing system developed at NOAA National Ice Center (NIC). IMS was designed to allow meteorologists to chart snow cover interactively on a daily basis using a variety of data sources within a common geographical system (Helfrich, McNamara, Ramsay, Baldwin, & Kasheta, 2007). IMS has historically been the most widely used for operational mapping and climatological analysis of large-scale snow extents (Frei et al., 2012). A key feature of the IMS products is that human input remains an integral part of the process (Frei & Lee, 2010). IMS snow-cover products are often used for validation and comparison of snow-cover maps (Romanov et al., 2000; Siljamo & Hyvärinen, 2011). Hence, IMS snow-cover products were selected for validation of the proposed method developed in this work for monitoring snow cover.

3. Method

3.1. Data pre-processing

In this study, both FY-2D and FY-2E VISSR data were used for monitoring snow cover over China. Original FY-2D and FY-2E VISSR data were stored in Hierarchical Data Format (HDF) with a geostationary satellite normalized projection. All VISSR data was resampled to a 0.05° grid (approximately 5 km) to match the lower spatial resolution of the IR bands, which is also 5 km. VISSR data was reassembled on a latitude–longitude projection to facilitate comparison with MODIS and IMS snow-cover products. One visible band and three infrared bands were used in this work. Observations of reflectance in the visible band, and infrared band brightness temperatures were calibrated based on the calibration tables stored in the HDF file with other datasets. The brightness temperatures of IR1 (10.3–11.3 μm) and IR4 (3.5–4.0 μm) were used to estimate the reflectance of IR4 band (Allen et al., 1990).

Because geostationary satellite observations are available for a wide range of illumination conditions, different satellite observation angles needed to be considered. Surface conditions do not change dramatically in one day, and therefore reflectance is not highly variable. For the same area observed by a geostationary satellite, a change in the solar angle causes reflectance variations, especially in the visible band; thus angular correction of geostationary reflectance data is significant in snow-cover classification, and uncorrected reflectance data varies strongly during the day. In this work, the raw reflectance was corrected by dividing observed reflectance by the cosine of the solar zenith angle.

The VISSR data from FY-2D and FY-2E satellites is different due to sensor degradation and the difference in their operational times: for FY-2D VISSR, daily observations begin at 00:30 UTC, with one hour temporal resolution; for FY-2E VISSR, start time is 00:00 UTC, with one hour temporal resolution. Imaging times for the two satellites coincide only at 05:30 UTC on any given day. Since the snow-cover algorithm below was developed based on the VISSR data from both satellites, cross-calibration of FY-2D and FY-2E data was carried out for the 05:30 UTC observation for the periods December 1–7, 2010, and December 1–7, 2011. The first period was used to cross-calibrate the VISSR data for the 2010 winter season (December 2010–February 2011). In order to reduce the effect of satellite sensor degradation, VISSR data for the second period was cross-calibrated for the 2011 winter season (December 2011–February 2012).

In the relative cross-calibration of FY-2D and FY-2E VISSR data, the corrected reflectance of visible and IR4 bands and the brightness temperatures of three IR bands (IR1, IR2 and IR4) were compared from linear relationships between VISSR data for FY-2D and FY-2E determined from scatter plots ($r^2 > 0.94$ for both time periods). The linear regression coefficients were similar for the two periods. To test these, we examined the VISSR data from both satellites for the periods February 1–7, 2011 and February 1–7, 2012. The results showed that the cross-calibration reduced the difference between FY-2D and FY-2E VISSR data to <0.02 for the visible and IR4 band reflectance, and <2.3 K for the three IR bands. Both the FY-2D and FY-2E VISSR data were then used in the development of a snow-cover algorithm that takes the differences in account.

3.2. Snow-cover algorithm development

Snow cover exhibits a specific spectral characteristic compared to other natural surfaces and clouds, with high reflectance in the visible band similar to that of clouds. In the short-wave band (1.6 μm) it has lower reflectance than clouds. Discrimination between snow and cloud cover is a crucial procedure in snow-cover algorithms. The Normalized Difference Snow Index (NDSI) is widely used for snow detection on the 0.6 μm and 1.6 μm channels; however, since the VISSR on FY-2D/E lacks a 1.6 μm channel, NDSI cannot be used for snow-cover detection. Of the currently operational geostationary satellites, only MSG is equipped with the 1.6 μm channel; GOES and MTSAT-2 do not have this facility.

Most operational snow-cover algorithms based on geostationary satellites are empirically based on the reflectivity characteristics of samples collected from different surface types (Siljamo & Hyvärinen, 2011). Romanov et al. (2000, 2003) used the Snow Index (SI), which they defined as the VIS:MIR ratio 0.6:3.9 μm reflectance, and other thresholds

Table 1
FY-2 VISSR band information.

Band	Wavelength range (μm)	Spatial resolution (km)	Radiometric resolution (bit)
VIS	0.55–0.90	1.25	6
IR1	10.3–11.3	5	10
IR2	11.5–12.5	5	10
IR3	6.3–7.6	5	10
IR4	3.5–4.0	5	10

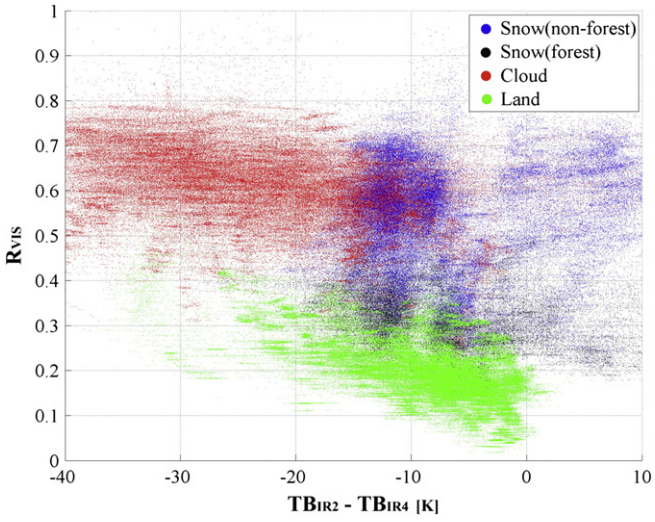

Fig. 2. Example of scatter plot from the development datasets.

for GOES snow-cover detection. Brightness temperature differences of 3.9, 10.9, 12.0 and 3.9 μm have been used to discriminate between clouds and snow (Siljamo & Hyvärinen, 2011; Wildt et al., 2007).

The snow mapping technique for VISSR developed in this study incorporates a threshold-based algorithm discriminating between snow-covered surfaces, snow-free surfaces, and clouds. Four VISSR channels (0.6, 3.9, 10.9 and 12.0 μm) were used in the snow-cover algorithm. SI, difference in IR2 and IR4 brightness temperatures (ΔT_B1), and difference in IR2 and IR1 brightness temperatures (ΔT_B2) were used to discriminate between clouds and snow-covered surfaces. The reflectance in the visible spectral band (R_{VIS}), IR4 band (R_{IR4}), and the brightness temperature of IR1 band ($T_{B\ IR1}$) were also used.

In developing the snow-cover algorithm, samples of observations of snow-covered surfaces, snow-free surfaces and cloud were collected; the VISSR observations of both FY-2D and FY-2E in year 2010 were used. The snow-covered surface sample selection consisted mainly of observations during the snow season January–March and November–December, 2010. Reflectivity of snow-covered forests differs from other snow-covered surfaces, so snow-covered surfaces were categorized as either forest or non-forest surfaces. The forest land-cover type was determined from the MODIS land-cover map (MCD12Q1) for 2009, which is a combination of Land Cover Type Yearly L3 Global 500 m SIN Grid version 005 from the Terra and Aqua satellites. Meteorological station observations were used to collect the training samples of snow-covered surface and snow-free surface. The observation information provided by meteorological stations included daily snow depth, daily air temperature and other parameters. When the snow depth is >0, the corresponding pixel containing that station was treated as a snow-covered surface, and when snow depth = 0, the corresponding pixel was treated as a snow-free surface. FY-2D and FY-2E cloud images (nephograms) were used to collect the training samples of clouds by visual identification and analysis; this is possible since, in general, cloud movement discriminates clouds from other surface types.

The FY-2D/E snow-cover algorithm was developed by analyzing scatterplots and histograms of various spectral indices and thresholds values. Figs. 2 and 3 are examples of scatterplot and histograms of the training samples. Fig. 2 shows the scatterplot of reflectance at 0.6 μm (*y*-axis) and difference in brightness temperature between IR2 and IR4 (*x*-axis). In Fig. 2, the non-forest snow-covered surface and clouds both show higher visible reflectance than forest snow-covered surface and snow-free surfaces, with the snow-free surface having the lowest visible reflectance; snow-covered surface has higher brightness IR2

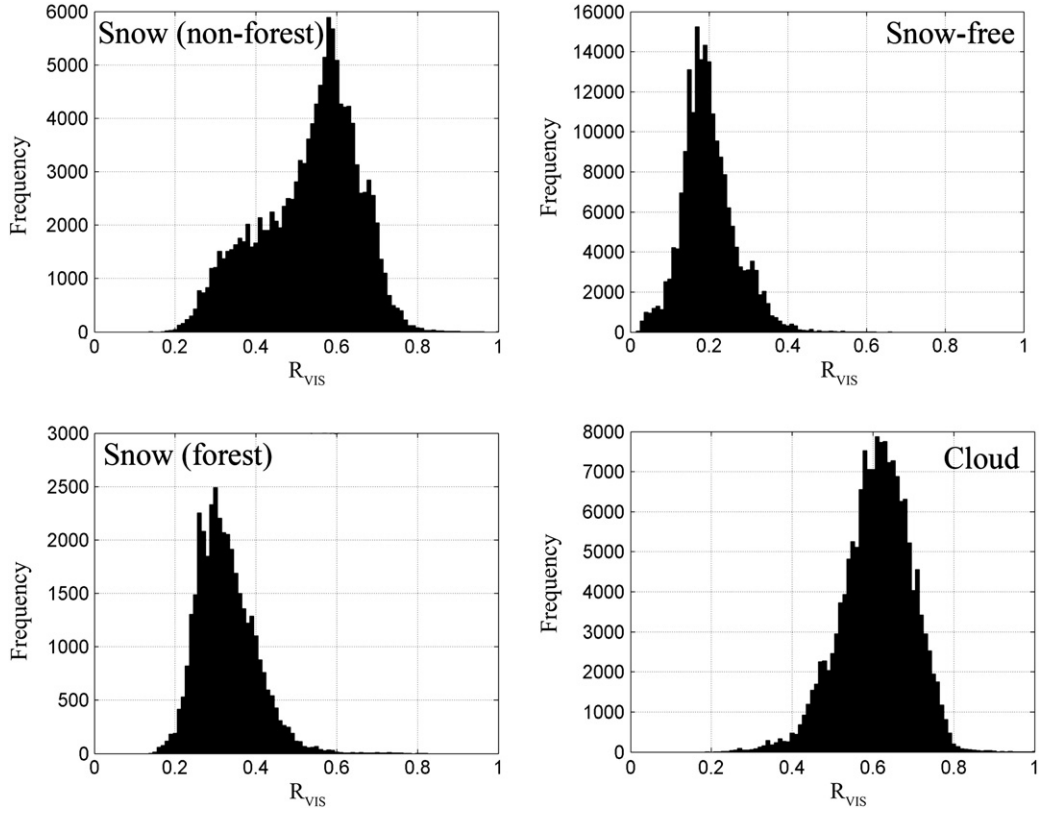

Fig. 3. Example of histograms of the development datasets.

and IR4 temperature differences than either snow-free surface or clouds.

Histograms of the snow detection indices for each channel were also used to set the threshold of the snow-cover algorithm. Fig. 3 shows the different distributions of the four categories of the training samples, confirming that the snow-free surface has a lower R_{VIS} than either clouds or snow-covered surfaces.

Some pixel thresholds were directly classified from Figs. 2 and 3, but pixels with similar spectral characteristics could not be classified correctly in this way. For example, both the clouds and the snow-covered surfaces show high reflectance in the 0.6 μm channel. In this study, the snow-cover algorithm consisted of two phases. Both phases are based on the threshold classifications.

Phase 1 comprised the spectral characteristics of snow-covered surfaces, snow-free surfaces and clouds. Table 2 lists the 12 classification rules for the algorithm: rules 1–4 discriminate between the snow-free surfaces from other surface types; rules 5 and 6 identify the snow-covered surfaces; and rules 7–12 detect clouds. Each pixel was tested sequentially for compliance with the rules and categorized accordingly. Pixels that satisfied more than one rule in the algorithm were placed in the category corresponding to the last rule in the sequence that it satisfied. To reduce the misclassification of snow-covered surfaces as clouds, the cloud classification rules are in the final sequence (rules 7–12).

The rules and thresholds were applied rigorously to ensure that the classifications were accurate. For rule 1, a pixel was classified as snow-free when $T_{BIR1} \geq 293$ K (determined from the histograms of the snow-free surface). For rule 5, a pixel was classified as snow-covered if it satisfied both $\Delta T_B1 \geq 3$ K and $R_{VIS} \leq 0.5$ (mainly based on combined scatterplot of ΔT_B1 and R_{VIS} in Fig. 2). When $\Delta T_B1 \geq 3$ K some cloud may be present, and it may also be present at higher R_{VIS} values than for a snow-covered surface; hence a combination of ΔT_B1 and R_{VIS} was used to classify the snow-covered surface.

When none of the rules in phase 1 were satisfied, the pixel was classified by the phase 2 snow-cover algorithm, which is a decision-tree spectral classification (Fig. 4) and supplements phase 1. In phase 2, to be classified as a snow-covered surface, a pixel must satisfy the five rules concurrently, i.e. SI, R_{VIS}, R_{IR4}, T_{BIR1} and ΔT_B1; if it does not, it is classified as cloud or snow-free surface (Fig. 4). The snow-cover algorithm allows hourly FY-2D and FY-2E VISSR snow-cover images to be captured. The algorithm is further discussed in Section 4.

A surface-temperature climatological test to reduce the overestimation of snow cover in seasonally snow-covered areas (Romanov & Tarpley, 2003) was applied following classification. In this work, the test adopted the average monthly surface temperature as the test criterion. Surface temperature data was obtained from the seven-year (2003–2009) MODIS monthly land surface temperature product MODIS/Terra Land Surface Temperature and Emissivity (LST/E) Monthly L3 Global 0.05° CMG (known as MOD11C3). For cloud pixels, large differences were evident between the scene brightness temperature and corresponding climatic surface temperature. In this work, if a pixel had an infrared brightness temperature T_{BIR1} more than 20 K below the climatic surface temperature, the pixel was reclassified as cloud. However, for occasional snowfall events, such as the heavy snowfalls in southern China in 2008, this surface temperature test may underestimate snow cover (Riggs & Hall, 2012).

Table 2
Snow cover algorithm of FY-2D/E (phase 1).

Threshold	Classification	Rule number
$T_{B\ IR1} \geq 293$ K	Snow-free	1
$R_{VIS} \leq 0.2$ & $R_{IR4} \geq 0.25$	Snow-free	2
$R_{VIS} \leq 0.16$	Snow-free	3
$\Delta T_B1 \leq -6$ K & $R_{VIS} \leq 0.2$	Snow-free	4
$\Delta T_B1 \geq 3$ K & $R_{VIS} \leq 0.5$	Snow-covered	5
$\Delta T_B1 \geq 10$ K & $T_{B\ IR1} \geq 250$ K	Snow-covered	6
$\Delta T_B1 \leq -38$ K	Cloud	7
$T_{B\ IR1} \leq 233$ K	Cloud	8
$\Delta T_B1 \leq -23$ K & $SI \geq 4$	Cloud	9
$R_{VIS} \geq 0.6$ & $R_{IR4} \geq 0.6$	Cloud	10
$\Delta T_B1 \leq -20$ K & $T_{B\ IR1} \leq 240$ K	Cloud	11
$\Delta T_B2 \geq 12$ K	Cloud	12

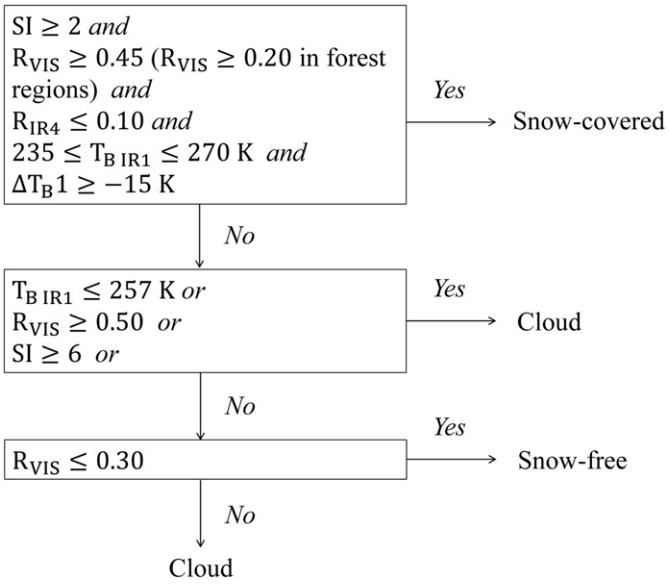

Fig. 4. Snow cover algorithm of FY-2D/E (phase 2).

3.3. Daily composite of snow-cover image

Based on the snow-cover algorithm above, FY-2D and FY-2E VISSR snow-cover images were obtained every hour. During daylight, hourly snow-cover images of FY-2D and FY-2E provide simultaneous snow-cover information. The daily combined snow-cover image was obtained by combining the hourly FY-2D and FY-2E VISSR snow-cover images. In the present work, the hourly snow-cover images following surface temperature climatological testing were used to produce the daily snow cover image.

The composition of the hourly FY-2D and FY-2E VISSR snow-cover images was based on the priority principle — that is, low-priority classification results were replaced, pixel by pixel, by higher-priority classifications, similar to the process usually adopted for MODIS snow-cover products (Gao et al., 2010). The order of priority was snow-covered surface > snow-free surface > cloud; thus, every pixel classified as 'snow-covered', 'snow-free' or 'cloud' in an FY-2D or FY-2E VISSR hourly snow-cover image was set to the corresponding classification in the combined image. Combining the images in this way over the period of one day decreases cloud obscuration and consequently help obtaining more information about the surface. The daily snow-cover FY-2D and FY-2E composite image is referred to as FY_2DE in the following analysis.

3.4. Generating cloud-clear snow map

It is possible to reduce cloud obscuration in an optical snow-cover image by spatial–temporal filtering, whereby cloud pixels are reclassified using the information from neighboring non-cloud-covered pixels in space or time, or by combining snow-cover images from different platforms or satellites (Parajka, Pepe, Rampini, Rossi, & Blöschl, 2010). Although the high temporal resolution of FY-2D/E VISSR data reduces cloud contamination, some cloud cover still appears in the images. To obtain cloud-free images, spatial–temporal filtering techniques and multi-sensor methodology were utilized to remove cloud obscuration completely.

3.4.1. Spatial–temporal filtering

The spatial filtering used in this study is similar to that of previous studies that were mainly focused on improving MODIS snow-cover products (Parajka & Blöschl, 2008; Paudel & Andersen, 2011). Spatial filtering reclassifies a cloud pixel as either 'snow cover' or 'snow free' if the eight neighboring pixels are all correspondingly 'snow cover' or 'snow free'.

Temporal filtering examines the classifications of every cloud pixel for the previous day and for the next day, and is used to check whether or not the pixel was snow covered: if the 'snow cover' or 'snow free' classification for that pixel occurred on both the previous day and the following day, it was reclassified accordingly. An FY_2DE snow-cover image filtered in this way is denoted FY_2DE_ST. Spatial–temporal filtered images are not in real time, since temporal filtering uses information from both the previous day and the following day.

3.4.2. Blended FY-2D/E VISSR and FY-3B MWRI snow cover

Although multi-temporal FY-2D/E VISSR data and spatial–temporal filtering were used in snow-cover mapping to remove the obscuring effect of extensive cloud cover, some cloud contamination may still exist. In these conditions, FY-3B MWRI data was used. Current algorithms for passive microwave remote sensing of snow depth fail to identify wet snow in southern China (Jin & Chen, 2011). In the present study, the improved snow-cover identification method proposed by Li, Liu, Zhu, Zheng, and Chen (2007) was used. This method, which has been found to perform well over China, utilizes meteorological station observations and SSM/I brightness temperature data to improve the snow-cover algorithm proposed by Grody and Basist (1996). The horizontal polarization difference of ascent and descent at 36.5 GHz has been demonstrated to detect wet snow (Ramage & Isacks, 2003). If snow is dry during the night and becomes wet during the day, then brightness temperatures obtained during the day will be higher than those obtained at night. The horizontal polarization brightness temperature at 36.5 GHz shows large day/night differences, so the snow-cover algorithm was improved by utilizing differences of more than 10 K to detect wet snow in southern China. Because FY-3B MWRI data does not cover all of China on a daily basis, the missing data is supplemented by the previous day's data to complete the coverage.

FY_2DE_ST and FY-3B MWRI snow-cover images were blended on a pixel-by-pixel basis. FY_2DE_ST images were used in cloud-free situations, and FY-3B MWRI images were blended in cloud-obscured situations. Remaining cloud-covered pixels in the FY_2DE_ST images were reclassified on the basis of the FY-3B MWRI data. The combined FY_2DE_ST and FY-3B MWRI snow-cover images are named FY_2DE_FM in the following analysis.

3.5. Evaluation of snow-cover images

The accuracy of the snow-cover images was quantitatively evaluated using meteorological ground station observations, considered as ground truth. A total of 699 such observations provided by the CMA were used. Errors due both to under- and overestimation are widely used in assessing misclassification of remote sensing images (Gao et al., 2010). In this work, errors were assessed in terms of image underestimation (IU, image misclassification as snow-covered instead of snow-free) and overestimation (IO, image misclassification as snow-free instead of snow-covered). Overall agreement between satellite snow-cover images and station observations is represented in this work by an accuracy index of overall accuracy, O_A, which is defined as the sum of the correct classification of station observations by snow-cover images, and includes the correct classification of snow-covered and snow-free surfaces. IU, IO and O_A are expressed below (as percentages):

$$\mathrm{IU} = \frac{b}{a+b+c+d} \tag{1}$$

Table 3
Confusion matrix for remote sensing image vs. station observations.

	Image: snow	Image: no snow
Station: snow	*a*	*b*
Station: no snow	*c*	*d*

$$\mathrm{IO} = \frac{c}{a+b+c+d} \tag{2}$$

$$\mathrm{O}_A = \frac{a+d}{a+b+c+d} \tag{3}$$

where *a*, *b*, *c* and *d* are the number of station observation pixels in each classification category. For detailed definitions of *a*, *b*, *c* and *d*, see Table 3.

4. Results and discussion

4.1. Comparison of FY-2D/E and MODIS snow-cover maps

MODIS snow-cover products under clear skies are consistent with available satellite- and ground-based snow datasets (Parajka & Blöschl, 2008). Cloud obscuration is the main limitation of MODIS snow-cover products. In this work, daily MOD10A1 and MYD10A1 snow-cover products were compared with FY-2D/E images. (MODIS/Terra or MODIS/Aqua Snow Cover 5-Min L2 Swath 500 m provide more snow-cover scenes per day, especially in northern China. Here, however, we chose MOD10A1 and MYD10A1 for their ease of processing and comparison.)

To match the spatial resolution of FY-2D/E, both the MOD10A1 and MYD10A1 snow-cover datasets were re-projected and resampled to 0.05° grid size using the MODIS Reprojection Tool (MRT). The nearest-neighbor resampling approach was employed when using the MRT tool. These combined Terra and Aqua MODIS daily snow-cover products (denoted as MODIS_DC) reduces cloud obscuration to some extent (Wang et al., 2008). The same priority principle (Gao et al., 2010) was adopted as above; that is, snow-covered surface > snow-free surface > cloud. When a pixel in either MOD10A1 or MYD10A1 represented a snow-covered surface, snow-free surface or cloud, the MODIS_DC pixel was set accordingly.

The FY_2DE snow-cover images were compared with the corresponding MODIS_DC snow-cover images on a pixel-by-pixel basis. Fig. 5 shows the comparative FY_2DE and MODIS_DC snow-cover images for January 10, 2011. It can be seen that MODIS_DC image shows significantly more cloud obscuration than the FY_2DE image. Consistent cloud-free conditions are seen for north-eastern and north-western China for both images. The higher daily temporal resolutions of FY-2D and FY-2E data (more than 20 images per day) are seen to have removed more cloud obscuration and obtained more information on the surface properties than MODIS_DC (only two images per day). Fig. 6 presents the time-series cloud coverage percentages of FY_2DE and MODIS_DC snow-cover images for two winter seasons (December 1, 2010–February 28, 2011, and December 1, 2011–February 29, 2012). The average cloud percentages over the two winter seasons for the FY_2DE and MODIS_DC snow-cover images respectively were approximately 16.28% and 46.75%.

A detailed comparison of FY_2DE and MODIS_DC snow-cover images is given in Table 4. The percentage of each category is the average value over a total of 181 days for the two winter seasons. The percentages of FY_2DE and MODIS_DC are similar (approximately 62.82%), being either snow-covered, snow-free or cloud. The main difference between the FY_2DE and MODIS_DC images concerns the amount of cloud obscuration. Cloudy conditions in MODIS_DC and snow-covered

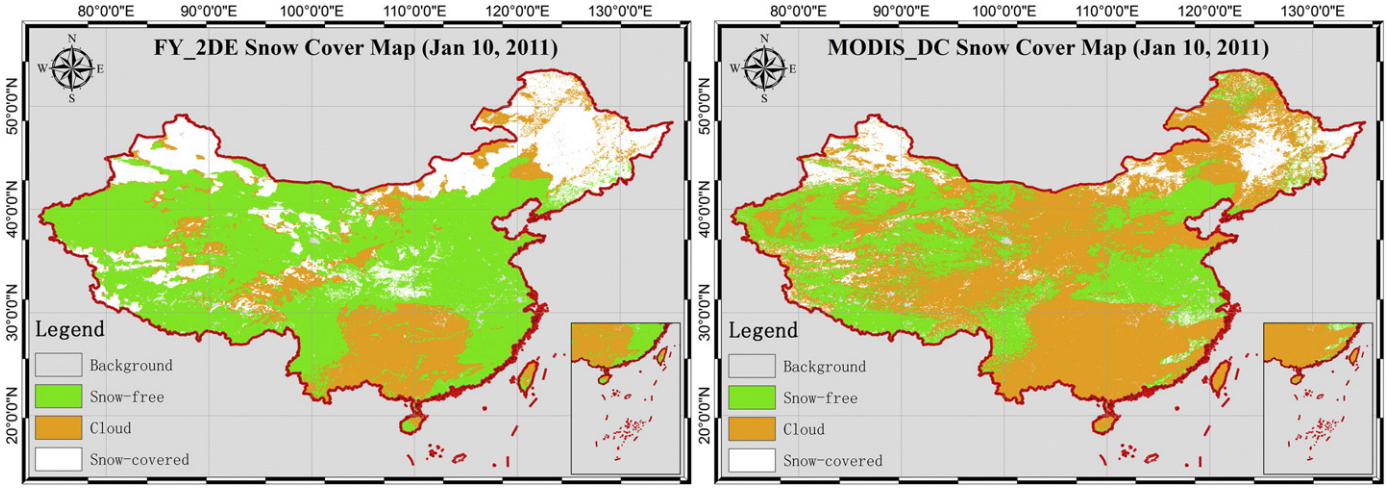

Fig. 5. FY_2DE and MODIS_DC snow cover images on January 10, 2011.

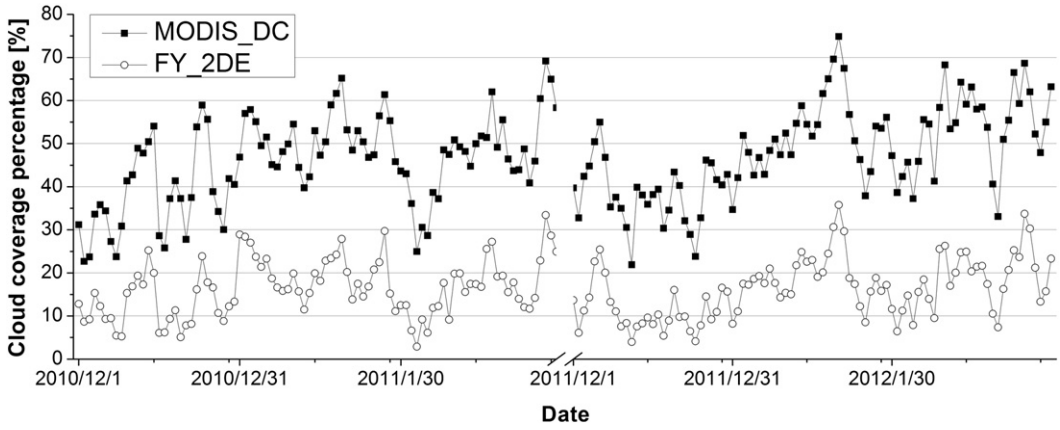

Fig. 6. Cloud coverage percentages of FY_2DE and MODIS_DC snow cover images from December 1, 2010, to February 28, 2011, and December 1, 2011, to February 29, 2012.

conditions in FY_2DE constitute approximately 10.20%. Snow-free conditions in FY_2DE and cloudy conditions in MODIS_DC are approximately 21.39%.

4.2. Validation with ground observations

In this work, observations from 699 meteorological stations across China were used to evaluate the snow-cover images of FY_2DE_ST, FY-3B MWRI, FY_2DE_FM and IMS for the winters of 2010–2011 and 2011–2012 (December 1, 2010–February 28, 2011, and December 1, 2011–February 29, 2012). The images for January 10, 2011 are shown as examples in Fig. 7. FY_2DE_FM is the composite image based on FY_2DE_ST and FY-3B MWRI. The overall accuracy (O_A) and classification error (IU and IO) of the four images were calculated from ground observations.

Table 4
Comparison of FY_2DE and MODIS_DC snow cover images.

FY_2DE	MODIS_DC	Percentage [%]
Snow-covered	Snow-covered	7.69
Snow-covered	Snow-free	2.18
Snow-covered	Cloud	10.20
Snow-free	Snow-covered	2.29
Snow-free	Snow-free	39.96
Snow-free	Cloud	21.39
Cloud	Snow-covered	0.57
Cloud	Snow-free	0.55
Cloud	Cloud	15.17

Fig. 8 is a time series of the overall accuracy (O_A) of the four images. This confirms that FY-3B MWRI was the least accurate of the four, due to the coarse spatial resolution of passive microwave data. The average overall accuracy of FY-3B MWRI in the two winter seasons was approximately 86.18%. The trends and overall accuracies of the FY_2DE_ST, FY_2DE_FM and IMS images were similar, at approximately 91.76%, 91.28% and 92.51%, respectively. The overall accuracy of FY_2DE_FM was a little lower than that of FY_2DE_ST due to its combination with the less-accurate FY-3B MWRI. The overall accuracy of FY_2DE_FM also depends on the cloud-covered areas in FY_2DE_ST snow-cover images. The overall accuracy difference between the FY_2DE_FM and IMS images was approximately 1%, indicating that the FY_2DE_FM images were highly accurate.

The underestimated (IU) errors of the FY_2DE_ST, FY-3B MWRI, FY_2DE_FM and IMS images for the two winter seasons are shown in Fig. 9. The average IU error percentage was approximately 2.25%; the IMS snow-cover image produced the lowest IU error. As well as higher IU average errors, the FY_2DE_ST, FY-3B MWRI and FY_2DE_FM images also showed some variation: 5.41% for FY_2DE_ST, 5.22% for FY-3B MWRI and 5.82% for FY_2DE_FM. Underestimation of snow cover in the FY-3B MWRI images in wet snow conditions also led to a higher IU error for FY_2DE_FM.

Fig. 10 shows the overestimation (IO) errors. The FY-3B MWRI images show the highest IO error percentage, averaging approximately 8.59%. The main contributor to the high IO error for FY-3B MWRI images

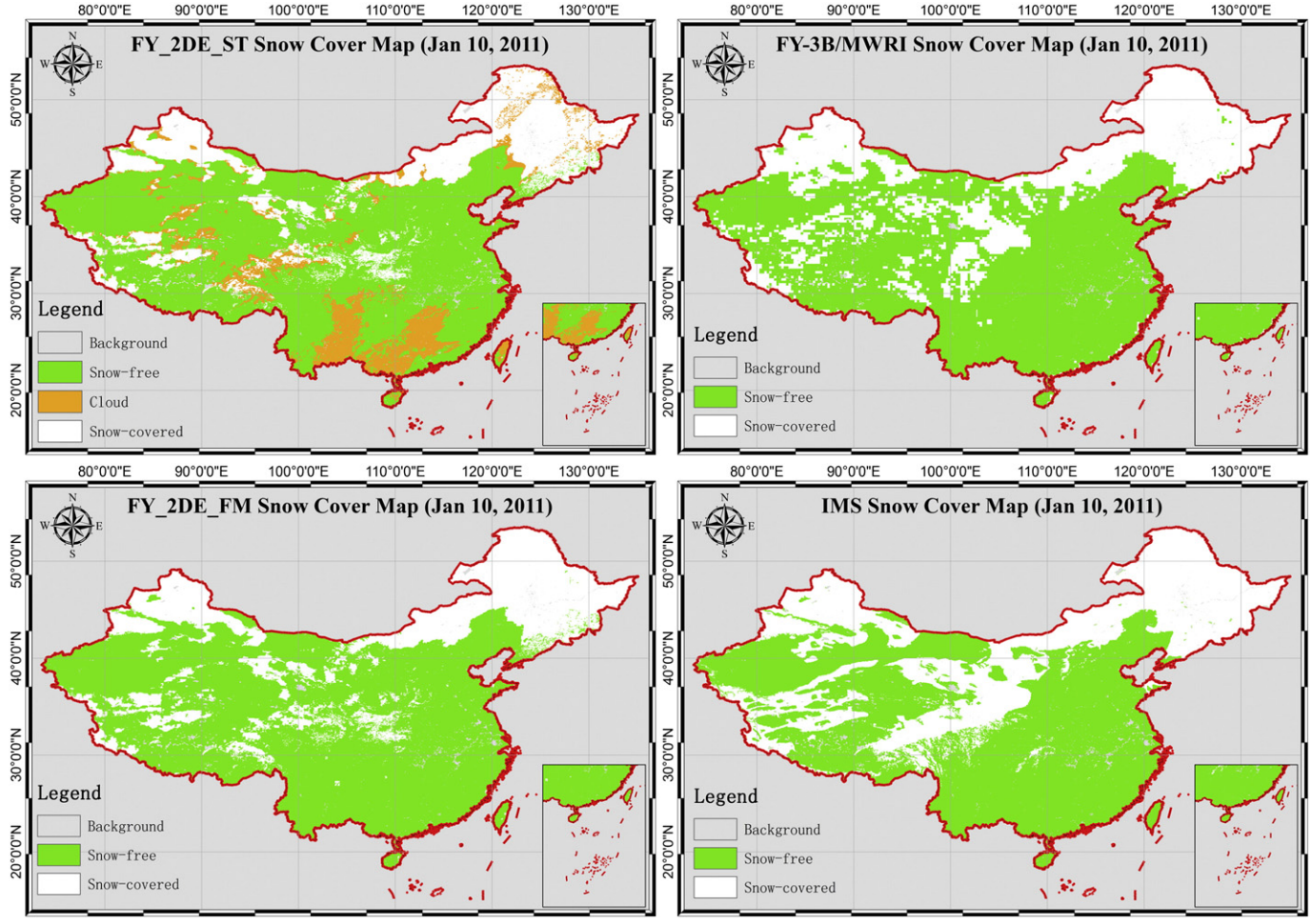

Fig. 7. Snow cover images of FY_2DE_ST, FY-3B MWRI, FY_2DE_FM and IMS on January 10, 2011, over China.

is again the coarse spatial resolution of MWRI data. In contrast to its low IU error, the IMS images show a higher IO error than either FY_2DE_ST or FY_2DE_FM. The average IO errors were approximately 5.23% for IMS, 2.83% for FY_2DE_ST and 2.90% for FY_2DE_FM.

Hall and Riggs (2007) summarized the overall absolute accuracy of daily MODIS snow-cover products as about 93% in clear sky conditions. Huang, Liang, Zhang, and Guo (2011) showed that the snow-cover mapping correspondence between the MODIS eight-day snow-cover composite product MOD10A2 and surface observations was 94.6% in northern Xinjiang, China. The accuracy of GOES + SSM/I composite snow-cover products over North America was 85% when compared with ground station data (Romanov et al., 2000). Simic, Fernandes, Brown, Romanov, and Park (2004) showed that the average agreement in Canada between MOD10A1 snow-cover products and field measurements was 93%, and 92% for the GOES + SSM/I snow-cover products. When compared with field measurements, the accuracy of MSG SEVIRI snow-cover maps over Europe was 88%, 96% and 95% for three datasets (Wildt et al., 2007).

In the present study, the average agreement between field observations and FY_2DE_ST images was 91.76%, and was 91.28% for

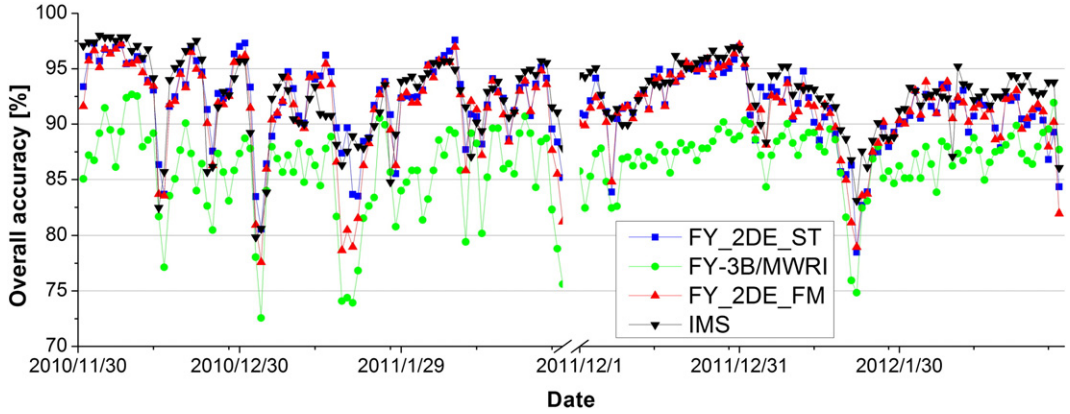

Fig. 8. Overall accuracy of snow cover images of FY_2DE_ST, FY-3B MWRI, FY_2DE_FM and IMS over China from December 1, 2010, to February 28, 2011, and December 1, 2011, to February 29, 2012.

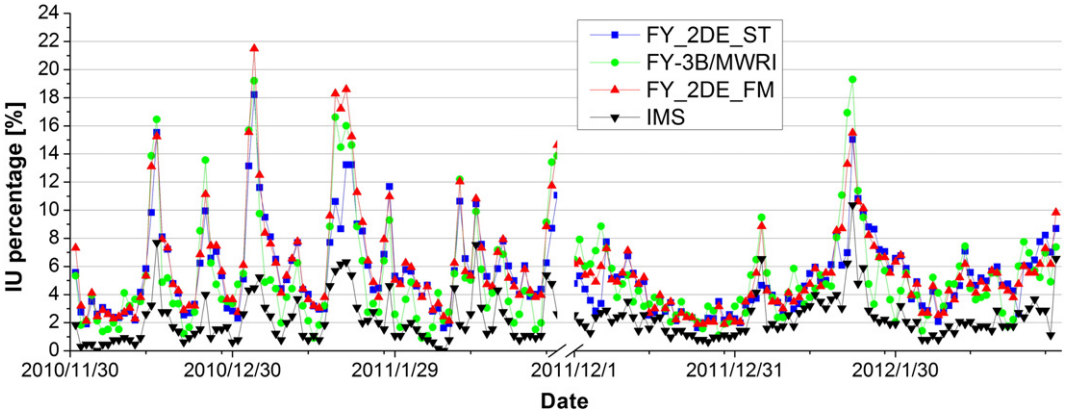

Fig. 9. Under-estimation error of snow cover images (IU) of FY_2DE_ST, FY-3B MWRI, FY_2DE_FM and IMS over China from December 1, 2010, to February 28, 2011, and December 1, 2011, to February 29, 2012.

FY_2DE_FM. The main reason for the slightly lower accuracy than current MODIS snow-cover products may be the lower spatial resolution and channel setting of the VISSR sensor; however, the FY_2DE_ST images have the advantage that they reduce cloud obscuration, and FY_2DE_FM images are unaffected by cloud obscuration.

4.3. Evaluation of the effect of elevation on the snow cover mapping accuracy

Because elevation affects snow-cover mapping, performances of the FY_2DE_ST, FY-3B MWRI, FY_2DE_FM and IMS snow-cover images for different elevation zones were analyzed. Fig. 11 shows the monthly under- and overestimation errors and overall accuracies of the different snow-cover images at different elevations. The error percentages (IU and IO) and overall accuracies (O_A) in clear-sky conditions were calculated separately for five elevation zones in which meteorological stations are located. IMS images had the lowest IU. Both FY_2DE_ST and FY_2DE_FM images showed high IU percentages in January 2011, mainly due to the underestimation of snow cover in southern China.

None of the snow-cover images showed a consistent relationship between elevation and underestimation errors. IO error percentages were low for FY_2DE_ST and FY_2DE_FM images in the two winter seasons; FY-3B MWRI images had the highest IO percentage. All snow-cover images exhibited the highest IO percentage at elevations of 2000 m and above. Most of the meteorological stations in that zone are located on the Tibetan Plateau. Both FY_2DE_ST and FY_2DE_FM snow-cover images showed low IO percentages in elevation zones below 2000 m.

As before, FY-3B MWRI images were the least accurate overall due to the coarse spatial resolution of passive microwave data. FY_2DE_ST images performed best of the four image types in terms of overall accuracy. The overall accuracies of FY_2DE_FM in the different elevation zones were slightly lower than those of FY_2DE_ST due to its combination with FY-3B MWRI images. In elevation zones below 1000 m, the IMS images showed a higher overall accuracy than FY_2DE_FM, but above 1000 m, this was reversed, although their overall accuracies were similar. In some elevation zones, FY_2DE_FM images were more accurate than IMS images.

4.4. Evaluation of the effect of land-cover types on the snow cover mapping accuracy

Landscape characteristics play an important role in the redistribution and physical properties of snow cover (Liang et al., 2008). The performances of the four image types were evaluated for different land-cover classes (Fig. 12). The MODIS yearly land-cover product was used in the assessment. The MCD12Q1 land-cover product (IGBP classification scheme) was reclassified in 2009 into four land-cover classes — forest, grassland, cropland and barren. Monthly IU, IO and O_A values for FY_2DE_ST, FY-3B MWRI, FY_2DE_FM and IMS images were compared.

FY_2DE_ST and FY_2DE_FM images showed similar IU percentages in both winter seasons, and IMS images showed the lowest IU error percentage overall. The four land-cover classes showed similar IU errors for IMS images. Grassland, cropland and barren land cover showed low IO errors for FY_2DE_ST and FY_2DE_FM images, with IO for forest being

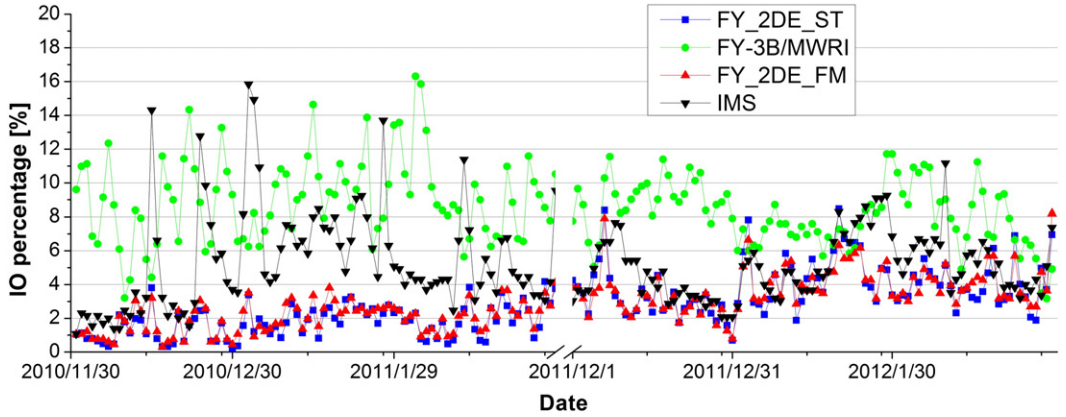

Fig. 10. Over-estimation error of snow cover images (IO) of FY_2DE_ST, FY-3B MWRI, FY_2DE_FM and IMS over China from December 1, 2010, to February 28, 2011, and December 1, 2011, to February 29, 2012.

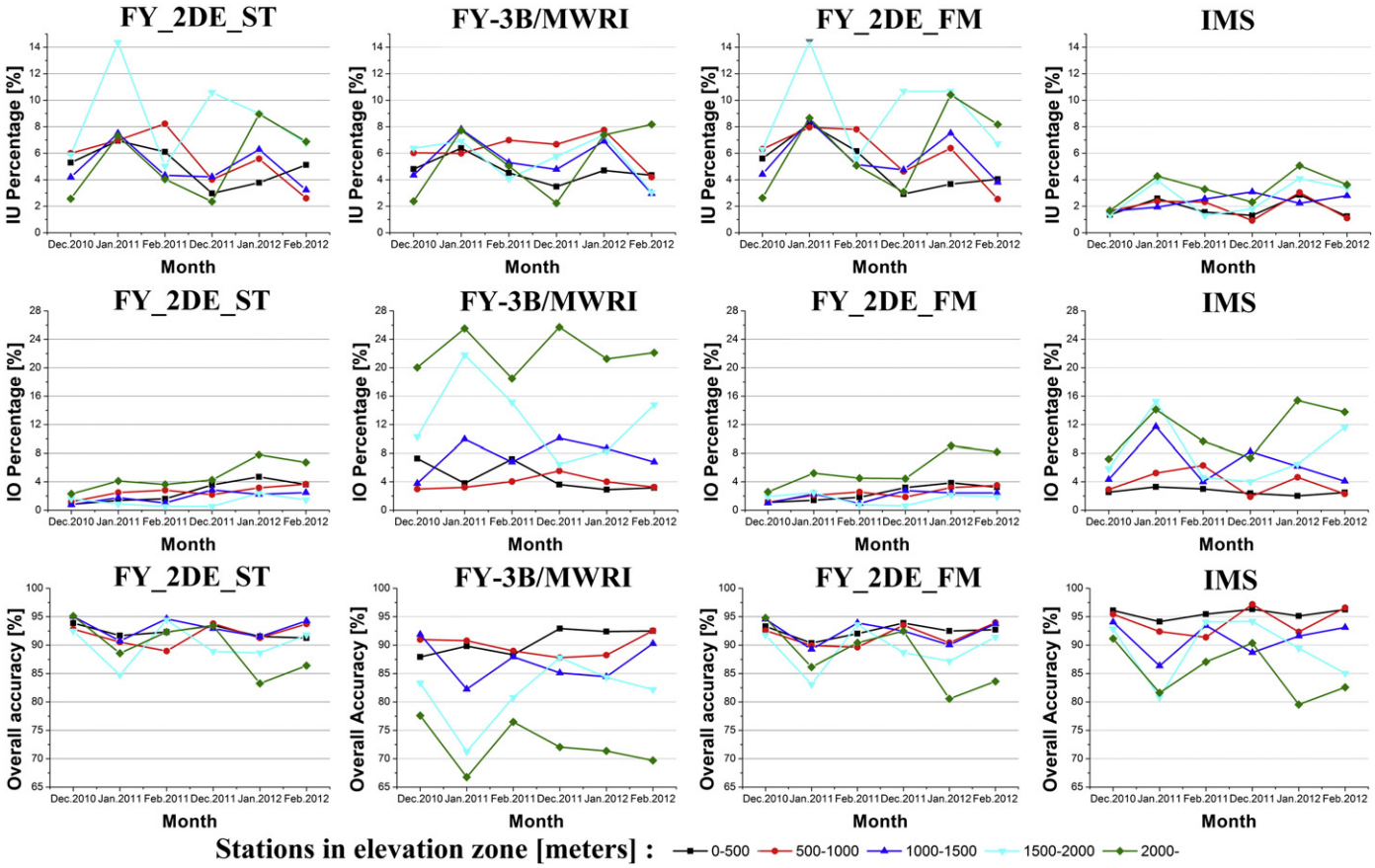

Fig. 11. The monthly under-estimation error (IU), Over-estimation error (IO) and overall accuracy (O_A) of FY_2DE_ST, FY-3B MWRI, FY_2DE_FM and IMS snow cover images in different elevation zones.

higher. FY-3B MWRI images showed higher IO errors than the other three image types.

The O_A of the four image types are also shown in Fig. 12. FY-3B MWRI images were the least accurate in all four land-cover classes. Again, this is due to the coarse spatial resolution of FY-3B MWRI data, so that snow-cover detection is less accurate than for the other optical snow-cover products. FY_2DE_ST and FY_2DE_FM snow-cover images in forest are the least accurate of the four land-cover classes; observed reflectance in forest areas is decreased because forests block the visibility of snow-covered surfaces, and the shadows of the trees also affect the images (Salminen, Pulliainen, Metsämäki, Kontu, & Suokanerva, 2009). The snow-cover algorithms used in FY-2D and FY-2E considered the effect of forest regions. We found that FY_2DE_ST and FY_2DE_FM images showed lower IU errors but higher IO errors in forested areas than in the other three land-cover classes. In FY_2DE_FM images, the overall accuracies were 87.53% for forest, 92.58% for grassland, 91.62% for cropland and 90.88% for barren land. For IMS images, these were 93.07%, 90.69%, 94.62% and 91.72% respectively.

In January 2011 and January 2012, the overall accuracies of FY_2DE_FM and IMS snow cover images decreased. The main reason for this appears to have been the greater number of snowfall events in China at those times. Snowfall in southern China always produces wet, shallow snow and despite the use of high-resolution temporal data with FY-2D and FY-2E, some areas continued to be obscured by cloud. In these regions, FY-3B MWRI snow-cover detection results dominated the FY_2DE_FM snow-cover image.

5. Conclusions

Geostationary satellite data with high temporal resolution is advantageous for monitoring snow cover. A high observation frequency can be used to monitor changes and capture all cloud-free surface characteristics over a single day. Geostationary satellites obtain more surface information than polar orbiters and with less cloud obscuration. In this study, data from the Chinese geostationary meteorological satellites FY-2D and FY-2E was combined for the first time to map snow cover over China. Taking into consideration snow-covered and snow-free surface along with cloud spectral characteristics, we have proposed a snow-cover algorithm based on FY-2D and FY-2E VISSR data. Although all FY-2D and FY-2E VISSR daily observations were used for snow cover mapping, clouds could not be completely removed from the images. Therefore, a spatial–temporal filter technique was used to remove clouds. In addition, FY-3B MWRI passive microwave data was also used for snow-cover mapping in cloud-obscured regions. Thus, a daily multi-sensor snow-cover map with minimal cloud obscuration was obtained.

FY_2DE snow-cover images have a lower cloud obscuration percentage than MODIS_DC images (16.28% and 46.75% respectively). Under clear sky conditions, the percentages of FY_2DE and MODIS_DC snow-cover images are similar, at approximately 91.42%. A detailed validation and comparison of FY_2DE_ST, FY-3B MWRI, FY_2DE_FM and IMS snow-cover images with meteorological station observations indicated that the overall accuracy of the FY_2DE_FM images was approximately 91.28%, compared to 92.51% for IMS images.

Taking elevation into consideration, we found that the FY_2DE_FM and IMS images showed similar overall accuracy in general. At some elevations, FY_2DE_FM images were superior to IMS images, but FY_2DE_FM images tended to slightly overestimate snow cover in forest regions. This aspect still needs to be improved.

Combining FY-2D/E VISSR and FY-3B MWRI data shows potential for monitoring snow cover over China with high accuracy. The method can used to detect snow-cover information with high temporal resolution

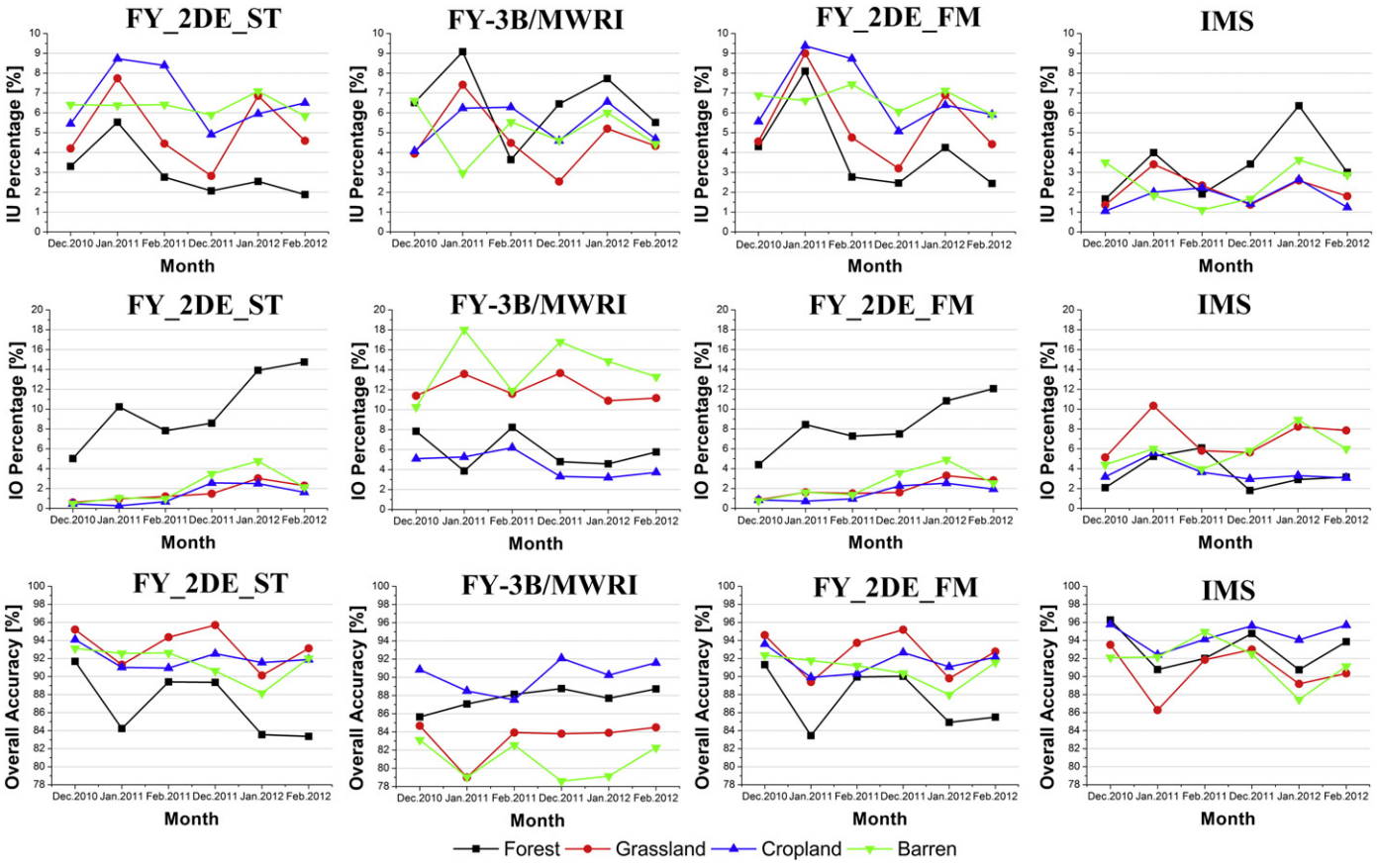

Fig. 12. The monthly under-estimation error (IU), Over-estimation error (IO) and overall accuracy (O_A) of FY_2DE_ST, FY-3B MWRI, FY_2DE_FM and IMS snow cover images in forest, grassland, cropland and barren land cover classes.

(approximately half an hour) and produce completely cloud-free snow-cover maps daily. In the near future, current snow-cover images will be extended to fractional snow cover.

Acknowledgments

This study is partly supported by the National Basic Research Program of China (No. 2013CB733406), National Natural Science Foundation of China (No. 41171260) and Beijing Higher Education Young Elite Teacher Project. The authors would like to thank China Meteorological Administration (CMA) and National Snow & Ice Data Center (NSIDC) for providing station observations, satellite data and products.

References

Allen, R. C., Durkee, P. A., & Wash, C. H. (1990). Snow/cloud discrimination with multispectral satellite measurements. *Journal of Applied Meteorology*, *29*(10), 994–1004.
Dozier, J., & Painter, T. H. (2004). Multispectral and hyperspectral remote sensing of Alpine snow properties. *Annual Review of Earth and Planetary Science*, *32*, 465–494.
Frei, A., & Lee, S. (2010). A comparison of optical-band based snow extent products during spring over North America. *Remote Sensing of Environment*, *114*(9), 1940–1948.
Frei, A., Tedesco, M., Lee, S., Foster, J., Hall, D. K., Kelly, R., et al. (2012). A review of global satellite-derived snow products. *Advances in Space Research*, *50*(8), 1007–1029.
Gao, Y., Xie, H., Lu, N., Yao, T., & Liang, T. (2010). Toward advanced daily cloud-free snow cover and snow water equivalent products from Terra–Aqua MODIS and Aqua AMSR-E measurements. *Journal of Hydrology*, *385*(1–4), 23–35.
Grody, N. C., & Basist, A. N. (1996). Global identification of snowcover using SSM/I measurements. *IEEE Transactions on Geoscience and Remote Sensing*, *34*(1), 237–249.
Hall, D. K., & Riggs, G. A. (2007). Accuracy assessment of the MODIS snow products. *Hydrological Processes*, *21*(12), 1534–1547.
Hall, D. K., Riggs, G. A., Foster, J. L., & Kumar, S. V. (2010). Development and evaluation of a cloud-gap-filled MODIS daily snow-cover product. *Remote Sensing of Environment*, *114*(3), 496–503.
Hall, D. K., Riggs, G. A., Salomonson, V. V., DiGirolamo, N. E., & Bayr, K. J. (2002). MODIS snow-cover products. *Remote Sensing of Environment*, *83*(1–2), 181–194.
Helfrich, S. R., McNamara, D., Ramsay, B. H., Baldwin, T., & Kasheta, T. (2007). Enhancements to, and forthcoming developments in the Interactive Multisensor Snow and Ice Mapping System (IMS). *Hydrological Processes*, *21*(12), 1576–1586.
Huang, X., Liang, T., Zhang, X., & Guo, Z. (2011). Validation of MODIS snow cover products using Landsat and ground measurements during the 2001–2005 snow seasons over Northern Xinjiang, China. *International Journal of Remote Sensing*, *32*(1), 133–152.
Jin, Y., & Chen, H. (2011). Detection of snow and frost in southern China in January 2008 using AMSR-E scattering and polarization indexes. *International Journal of Remote Sensing*, *32*(16), 4475–4487.
Li, X., Liu, Y., Zhu, X., Zheng, Z., & Chen, A. (2007). Snow cover identification with SSM/I data in China. *Journal of Applied Meteorological Science (in Chinese)*, *18*(1), 12–20.
Li, S., Yan, H., & Liu, C. (2007). Study of snow detection using FY-2C satellite data. *Journal of Remote Sensing (in Chinese)*, *11*(3), 406–413.
Liang, T. G., Huang, X. D., Wu, C. X., Liu, X. Y., Li, W. L., Guo, Z. G., et al. (2008). An application of MODIS data to snow cover monitoring in a pastoral area: A case study in Northern Xinjiang, China. *Remote Sensing of Environment*, *112*(4), 1514–1526.
Oyoshi, K., Takeuchi, W., & Yasuoka, Y. (2007). Evaluation of snow-cover maps over Northeastern Asia derived from AVHRR, MODIS and MTSAT data. *Proceedings of the 28th Asian Conference on Remote Sensing (ACRS). 12–16 November 2007, Kuala Lumpur, Malaysia*.
Parajka, J., & Blöschl, G. (2008). Spatio-temporal combination of MODIS images — Potential for snow cover mapping. *Water Resources Research*, *44*(3).
Parajka, J., Pepe, M., Rampini, A., Rossi, S., & Blöschl, G. (2010). A regional snow-line method for estimating snow cover from MODIS during cloud cover. *Journal of Hydrology*, *381*(3–4), 203–212.
Paudel, K. P., & Andersen, P. (2011). Monitoring snow cover variability in an agropastoral area in the Trans Himalayan region of Nepal using MODIS data with improved cloud removal methodology. *Remote Sensing of Environment*, *115*(5), 1234–1246.
Ramage, J. M., & Isacks, B.L. (2003). Interannual variations of snowmelt and refreeze timing on southeast-Alaskan icefields, U.S.A. *Journal of Glaciology*, *49*(164), 102–116.
Riggs, G. A., & Hall, D. K. (2012). Improved snow mapping accuracy with revised MODIS snow algorithm. *Proceedings of the 69th Eastern Snow Conference. 2012, Frost Valley YMCA, Claryville, New York, USA*.
Romanov, P., Gutman, G., & Csiszar, I. (2000). Automated monitoring of snow cover over North America with multispectral satellite data. *Journal of Applied Meteorology*, *39*(11), 1866–1880.
Romanov, P., & Tarpley, D. (2003). Automated monitoring of snow cover over South America using GOES Imager data. *International Journal of Remote Sensing*, *24*(5), 1119–1125.
Romanov, P., & Tarpley, D. (2007). Enhanced algorithm for estimating snow depth from geostationary satellites. *Remote Sensing of Environment*, *108*(1), 97–110.

Salminen, M., Pulliainen, J., Metsämäki, S., Kontu, A., & Suokanerva, H. (2009). The behaviour of snow and snow-free surface reflectance in boreal forests: Implications to the performance of snow covered area monitoring. *Remote Sensing of Environment*, *113*(5), 907–918.

Siljamo, N., & Hyvärinen, O. (2011). New geostationary satellite-based snow-cover algorithm. *Journal of Applied Meteorology and Climatology*, *50*(6), 1275–1290.

Simic, A., Fernandes, R., Brown, R., Romanov, P., & Park, W. (2004). Validation of VEGETATION, MODIS, and GOES + SSM/I snow-cover products over Canada based on surface snow depth observations. *Hydrological Processes*, *18*(6), 1089–1104.

USGS (1996). *GTOPO30 courtesy of the U.S. Geological Survey.*

Wang, X., Xie, H., & Liang, T. (2008). Evaluation of MODIS snow cover and cloud mask and its application in Northern Xinjiang, China. *Remote Sensing of Environment*, *112*(4), 1497–1513.

Wildt, M. R., Seiz, G., & Gruen, A. (2007). Operational snow mapping using multitemporal Meteosat SEVIRI imagery. *Remote Sensing of Environment*, *109*(1), 29–41.

Yang, H., Lv, L., Xu, H., He, J., & Wu, S. (2011). Evaluation of FY3B-MWRI instrument on-orbit calibration accuracy. *Proceedings of Geoscience and Remote Sensing Symposium (IGARSS), 2011 IEEE International. 24–29 July 2011, Vancouver, BC* (pp. 2252–2254).